Adhesion of ultrathin $ZrO_2(111)$ films on Ni(111) from first principles

A. Christensen[a)]
Department of Chemistry and Biochemistry, Box 951569, University of California, Los Angeles, California 90095-1569 and Center for Atomic-Scale Materials Physics (CAMP), Department of Physics, Technical University of Denmark, Bygning 307, DK-2800 Lyngby, Denmark

Emily A. Carter[b)]
Department of Chemistry and Biochemistry, Box 951569, University of California, Los Angeles, California 90095-1569

(Received 25 October 2000; accepted 10 January 2001)

We have studied the $ZrO_2(111)$/Ni(111) interface using the ultrasoft pseudopotential formalism within density functional theory. We find that $ZrO_2(111)$ adheres relatively strongly at the monolayer level but thicker ceramic films interact weakly with the Ni-substrate. We argue that the cohesion changes character from dominantly image charge interactions for thick ceramic films to more covalent for monolayer $ZrO_2(111)$ films. We provide an analysis of energetic, structural and electronic aspects of the ZrO_2/Ni interface as a function of the thickness of the oxide layer. We also address the role of the exchange-correlation density functional parameterization for modeling the oxide and metal/oxide interface and discuss the sensitivity of the supercell approximation for metal/oxide interface properties. © *2001 American Institute of Physics.*
[DOI: 10.1063/1.1352079]

I. INTRODUCTION

Characterization of the properties of crystalline interfaces between metals and ceramics is of fundamental interest—little is understood about the atomic level interactions at such interfaces[1]—and of practical interest—such interfaces are present in so-called thermal barrier coatings (TBC's). These coatings are used to protect gas turbine engine components found in both aircraft and stationary power plants. The protective coatings allow fuel combustion to be carried out at the highest possible operating temperature (maximizing fuel efficiency).[2] Unfortunately, current TBC's fail after a sequence of heating and cooling cycles.[3]

Zirconia-based materials are often chosen for TBC's, due to their high melting points, low thermal conductivity, similar coefficient of thermal expansion to that of Ni superalloys used to construct the engine parts, and excellent resistance to corrosion and thermal shock.[4,5] The main drawback of pure zirconia is the tetragonal-monoclinic phase transformation at 1180 °C, which is traversed at the desired operating conditions. This transition is accompanied by a volume expansion[6,7] of ~4%, which generates cracks and eventually de-adhesion of the TBC. The tetragonal-monoclinic transition is suppressed by adding cubic oxides in small amounts (~8.5%) to zirconia.[8,9] Still, TBC's are prone to thermal cycling fatigue, due to slightly unequal thermal expansion of the metal and the TBC, which causes the TBC to spall within the projected lifetime of the engine, as a result of thermally-induced stresses.[3] Other contributing mechanisms to the spallation are oxidation of the TBC/metal interface, enhanced by the relatively high oxygen anion mobility in zirconia and interface segregation of other species, activated at high temperatures. The spallation problem is often reduced by placing a bond coat in between the TBC and the metal, but under real life operating conditions, the bond coat is oxidized as well.[10,11] Therefore, a lot of effort[2,3] has been put into refining and optimizing TBC/bond coat/metal structures to meet engineering requirements. The search for design principles has hitherto been rather phenomenological; this is a consequence of the structural and chemical complexity of the TBC/bond coat/metal structures, together with the lack of nondestructive experimental probes for *in situ* atomic scale characterization of buried interfaces, let alone oxide surfaces. Our motivation for the paper is to understand at an atomistic level why one cannot simply deposit YSZ on Ni as a coating. Understanding this aspect provides a fundamental basis for optimizing bond coat properties. Furthermore, an atomistic level characterization of the zirconia/nickel interface system is also useful in other technological contexts, e.g., at anodes for solid oxide fuel cells.[12–17]

Atomistic modeling offers microscopic insight into otherwise inaccessible aspects of complex interface structures. Our group currently has a concerted effort to characterize, within ideal model interfaces, the interactions between different materials where they meet. Parallel to the present work, we also studied the ZrO_2/α-Al_2O_3 interface,[18] which is relevant to the TBC/bond coat interface, when the bond coat is oxidized. Also, this interface determines mechanical and thermal properties of technologically important ZrO_2/Al_2O_3 composites. We have also examined the Al_2O_3/Ni interaction,[19] where we learn that Al_2O_3 may be responsible for the spallation that occurs. We also previously studied the bulk and surfaces of all low pressure ZrO_2 phases.[20] Here, we concluded that the t-$ZrO_2(111)$ and the m-$ZrO_2(\bar{1}11)$ surfaces are most stable. This has implications

a)Electronic mail: asbjorn@chem.ucla.edu
b)Electronic mail: eac@chem.ucla.edu

for the tetragonal-monoclinic transition in ZrO_2 nanoparticles, explaining why the tetragonal structure is preferentially stabilized in small particles.

This paper is organized as follows: In Sec. II, we discuss the calculational details of our work and in Sec. II D we present test calculations with our set of input parameters for bulk ZrO_2 and Ni. In Sec. III, we start by discussing geometrical aspects of interface modeling (Sec. III A) and then we proceed with our results on structural features (Sec. III B), energetic aspects (Sec. III C), and electronic structure (Sec. III D) of the ZrO_2/Ni interface. Finally, in Sec. IV, we draw conclusions from our work.

II. CALCULATIONAL DETAILS

We study the ZrO_2(111)/Ni(111) interface by means of the ultrasoft pseudopotential formalism[21–23] within spin-polarized density functional theory (SDFT),[24–26] using the local spin density (LSDA) and generalized gradient (GGA) approximations for exchange and correlation effects.[27] The Kohn–Sham one-electron eigenstates are expanded in a plane wave basis subjected to periodic boundary conditions. All calculations are performed using the *ab initio* total-energy and molecular-dynamics program VASP (Vienna *Ab initio* Simulation Program) (Refs. 28–31) version 4.4 on both SGI Origin2000 and IBM/SP2 platforms.

A. The pseudopotentials

We used the ultrasoft pseudopotentials contained in database of the VASP code distribution, version 4.4. The Ni, Zr, and O pseudopotentials used in our study are of the nonlocal, separable Kleinman–Bylander form,[32] generated using a RRKJ scheme[33,34] to ensure optimally soft pseudopotentials, at a given transferability level. The local part of the pseudopotentials are taken as the all-electron potentials (unscreened with respect to the valence electrons) outside a suitably chosen radius r_{loc} from the nuclei and matched smoothly at r_{loc} to a zeroth order Bessel function, which is feasible to represent in a plane wave basis. Corresponding pseudopotential sets for Ni, Zr, and O exist in the database for both a LSDA and a GGA parameterization of the exchange-correlation density functional. The LSDA parameterization used is that of Perdew and Zunger,[35] based on the Monte Carlo results of Ceperley and Alder;[36] the GGA parameterization used is that of Perdew *et al.*[37,38] (conventionally labeled PW91). The same parameters for each of the elements, as summarized below, were used for generating the pseudopotential sets corresponding to the LSDA and the GGA.

The Ni pseudopotential is generated in the neutral $4s^1 3d^9$ configuration (which is the LSDA/GGA atomic ground state) with 10 electrons treated as valence. The outermost pseudization radius is $r_{\mathrm{ps}}=1.29$ Å (inside which the all-electron wave functions are smoothened). The local part of the pseudopotential is defined as described above, with $r_{\mathrm{loc}}=0.89$ Å. The *s*, *p*, and *d* angular channels were each augmented with two projectors generated at different reference energies. Partial core correction has been included in the Ni pseudopotential.

One Zr pseudopotential, referred to as $\mathrm{Zr_I}$ hereafter, is generated in the neutral $5s^1 4d^3$ configuration (which is the LSDA/GGA atomic ground state) with 4 electrons treated as valence. The outermost pseudoization radius is $r_{\mathrm{ps}}=1.62$ Å. The local part of the pseudopotential is defined as described above, with $r_{\mathrm{loc}}=1.27$ Å. The *s*, *p*, and *d* angular channels were each augmented with two projectors generated at different reference energies. It is well-known that Zr has semicore states, which influence the chemistry under certain circumstances. For the isolated Zr atom, the 4*s*, 4*p* states reside around 50 and 30 eV, respectively, below the atomic vacuum level. Here we investigate this issue for ZrO_2, using an alternative Zr pseudopotential, referred to as $\mathrm{Zr_{II}}$ hereafter, which includes the Zr(4*p*) electrons explicitly, so that this pseudopotential has 10 electrons treated as valence. It is generated with the same parameters as $\mathrm{Zr_I}$, except that the *p* channel is now augmented with an extra projector, generated at 34 eV below the atomic vacuum. Partial core correction has been included in both Zr pseudopotentials.

Traditionally, it has been a problem to generate tractable oxygen pseudopotentials, due to the deep 2*p* level; this situation has improved considerably with the introduction of ultrasoft pseudopotentials,[21] although still halogen and chalcogen elements often determine the necessary kinetic energy cutoff $E_{\mathrm{cut}}^{\mathrm{wf}}$ in the plane wave basis expansion in most practical situations. One soft O pseudopotential, referred to as $\mathrm{O_I}$ hereafter, is generated in the neutral $2s^2 2p^4$ configuration (which is also the LSDA/GGA and experimental atomic ground state) with six electrons treated as valence. The outermost pseudization radius is $r_{\mathrm{ps}}=1.00$ Å. The local part of the pseudopotential is defined as described above, with $r_{\mathrm{loc}}=0.54$ Å. The *s* and *p* angular channels were each augmented with two projectors generated at different reference energies. We also consider a harder O pseudopotential, generated with a slightly more conservative choice of parameters, supposedly increasing the transferability. We refer to this harder O pseudopotential as $\mathrm{O_{II}}$ in the following. It is also generated in the neutral $2s^2 2p^4$ configuration with six electrons treated as valence, but with an outermost pseudization radius $r_{\mathrm{ps}}=0.82$ Å. The local part of the pseudopotential is taken as the *d* channel pseudopotential [generated from the unbound O(3*d*) resonance]. As with $\mathrm{O_I}$, the *s* and *p* angular channels were each augmented with two projectors generated at different reference energies. Neither $\mathrm{O_I}$ nor $\mathrm{O_{II}}$ has a partial core correction added.

B. Electronic structure

In this section we summarize the algorithms and settings for determining the electronic ground state, represented by the Kohn–Sham one-electron eigenset. The total energies of relaxed structures are evaluated within collinear spin-density functional theory. Noncollinear effects are not expected to be important for the ZrO_2/Ni interface system, since the magnetism in Ni is well-reproduced with collinear, spin-polarized DFT and ZrO_2 is of course nonmagnetic.

For surface and interface calculations, a periodic supercell approach is used and the Brillouin zone integrals are performed on a $3\times3\times1$ Monkhost–Pack grid;[39] this corresponds to a sampling spacing $\kappa_{\mathrm{BZ}}=\sqrt{A_{\mathrm{BZ}}}/3=0.34$ Å^{-1},

which is empirically sufficient to represent dispersion features of *d*-band metals, like Ni; A_{BZ} is the area of the surface/interface Brillouin zone. This sampling corresponds to 5 *k*-points in the irreducible wedge of the Brillouin zone. ZrO_2 phases are insulating at low pressures and therefore Brillouin zone integrals are fairly well converged already at a sampling density ~ 0.6 Å^{-1}. To further enhance error cancellation with respect to Brillouin zone integral sampling, interface calculations and reference surface/bulk calculations (to determine, e.g., the surface and cohesive energy) are performed in unit cells with similar lattice vectors parallel to the interface and identical Monkhost–Pack grid indices (3×3) parallel to the interface. The electronic Fermi surface is broadened according to the scheme of Methfessel and Paxton,[40] using the first-order approximation to the step-function for occupation numbers. The width of the step-function is chosen to be $\sigma = 0.30$ eV, which preserves Fermi surface effects for most *d*-metals.[30,40] All energies reported in this paper are extrapolated analytically[30] to $\sigma = 0$.

The necessary kinetic energy cutoff, $E_{\text{cut}}^{\text{wf}}$, of the plane wave basis, in which the Kohn–Sham one-electron wave functions are expanded, is effectively determined by the oxygen pseudopotential in our case. In the ultrasoft pseudopotential formalism, a secondary kinetic energy cutoff $E_{\text{cut}}^{\text{aug}}$ comes into play. $E_{\text{cut}}^{\text{aug}}$ specifies the kinetic energy cutoff of the augmentation wave functions $\{\phi_i\}$ entering the augmentation density-matrix basis[21]

$$Q_{ij}(r) = \phi_i^*(r)\phi_j(r) - \tilde{\phi}_i^*(r)\tilde{\phi}_j(r), \tag{1}$$

where $\{\tilde{\phi}_i\}$ are the set of atomic ultrasoft pseudowave functions of the pseudoatom corresponding to the pseudopotential. Energy calculations using pseudopotential O_I were performed at $(E_{\text{cut}}^{\text{wf}}, E_{\text{cut}}^{\text{aug}}) = (270, 554)$ eV, whereas energy calculations involving the pseudopotential O_{II} were performed at $(E_{\text{cut}}^{\text{wf}}, E_{\text{cut}}^{\text{aug}}) = (396, 928)$ eV. These choices of $(E_{\text{cut}}^{\text{wf}}, E_{\text{cut}}^{\text{aug}})$ results for both pseudopotentials O_I and O_{II} in a convergence of the absolute total energies of about 0.1 eV/O-atom, whereas total energy *differences* are well converged within the accuracy of the calculation.

Generally speaking, the electronic density has Fourier components up to $4*\max(E_{\text{cut}}^{\text{wf}}, E_{\text{cut}}^{\text{aug}})$. For practical purposes, when choosing grids for the soft electronic pseudodensity, one may lower this bound to $3*\max(E_{\text{cut}}^{\text{wf}}, E_{\text{cut}}^{\text{aug}})$, without inducing considerable aliasing errors on high Fourier components. We used this approach in our calculations. One practical indicator of aliasing errors is the ionic force drift during the self-consistent cycles, which was below the convergence level (~ 0.05 eV/Å), set for terminating structural optimization cycles. A variant of a residual minimization and direct iterative subspace rotation method (RMM-DIIS) (Refs. 30, 31, 41) is used for finding electronic eigenstates iteratively. Twenty extra bands per *k*-point are included in all calculations, due to the metallic character of Ni and to accelerate the iterative minimization.

Our interface calculations primarily focus on the GGA for exchange-correlation effects (using the PW91 functional[37,38]) although some corresponding calculations are made using the LSDA (using the PZ parameterization[35]). We emphasize that in all our calculations, the atomic reference data (the pseudopotentials) and the multiatom calculations (based on pseudopotentials) have corresponding approximations for the exchange-correlation functional. In other words, we do not use, e.g., a pseudopotential set, generated with the LSDA, in a multiatom calculation with a GGA exchange-correlation functional for the electron density; this would constitute an ill-defined approximation.[42] Further, we note that self-consistent solutions to the Kohn–Sham equations were found for each density functional parameterization; i.e., GGA energies were not evaluated merely as a post-SCF-correction to the LSDA self-consistent solution.

C. Ionic relaxation

The supercell approach is used: surfaces are modeled as thin slabs, separated by vacuum. Interfaces are modeled as junctions between Ni and ZrO_2 slabs, separated by vacuum opposite the junction. This models ZrO_2 layers deposited on an infinite Ni substrate. We refer to Sec. III A for a more elaborate description our structural model of the interface. Ions are relaxed in all our interface and surface calculations to their equilibrium positions. Surface calculations are performed to assess the effects of forming the interface. No symmetry constraints are imposed on ionic relaxation, apart from the periodic boundary conditions inherent in the supercell formalism. The unit cell was not relaxed in interface calculations: it was considered pinned transversally by the Ni(111)-substrate. The lattice constant of the Ni(111)-substrate was fixed to that of the predicted equilibrium bulk value, corresponding to the actual exchange-correlation functional (LSDA or GGA) used; these values are discussed in Sec. II D.

Ions are relaxed using a conjugate gradient algorithm, until ionic forces are below ~ 0.05 eV/Å. Only the Ni-layer closest to the interface is allowed to relax (this applies to all interface calculations with both 3 and 4 layers of Ni substrate). The Ni-layers below are kept fixed to their crystalline bulk structure; this is done to avoid interaction of the interface with the free Ni surface on the other side of the Ni-slab via long-ranged displacement fields. We note *a postiori* that residual force components in lower Ni-layers are typically of order 0.1 eV/Å or less anyway, which is comparable to the convergence criterion for ionic minimization.

Determination of the equilibrium interface structures are done in three steps for efficient usage for computational resources:

(1) First, a rough structural minimization is performed. An initial guess of the interface structure is relaxed at a 25% lower planewave cutoff, $E_{\text{cut}}^{\text{wf}} = 203$ eV. We only performed interface calculations using the soft oxygen pseudopotential O_I; see Sec. II A. In practice, one finds that with pseudopotential calculations the equilibrium structure is well converged at a somewhat lower value of $E_{\text{cut}}^{\text{wf}}$ than necessary for the energy. A localized real-space representation[43] of the pseudopotentials summarized in Sec. II A is used; matrix elements of the nonlocal pseudopotential operator are evaluated much faster in real space for large systems, but this procedure is slightly inaccurate with realistic parameter settings. Further, the rough minimization calculations are per-

formed spin-paired. This is justified in light of the weak magnetism in Ni. With these bold settings, the systems are relaxed, using 50–150 ionic steps, so that forces are ~0.05 eV/Å.

(2) Second, the systems are relaxed further using more accurate settings. The planewave cutoff is raised to $E_{\text{cut}}^{\text{wf}} = 270$ eV, as mentioned in Sec. II A. Matrix elements of the nonlocal pseudopotential operator are evaluated rigorously in reciprocal space. The calculations are still performed spin-paired, since we find that the spin-structure coupling is rather negligible in the ZrO_2/Ni interface system; this is not unexpected, due to the weak magnetism of Ni. With these settings, the systems are further relaxed, using typically less than 5 ionic steps, until forces are converged below ~0.05 eV/Å.

(3) Finally, for the structure relaxed following these two steps, the total energy and density of states are evaluated using settings above, except that the calculation is performed spin-polarized. Forces are also evaluated, and it is confirmed that the structural minimization is converged, the forces being less than ~0.10 eV/Å. The same procedure is used in calculations for reference surfaces of Ni(111) and ZrO_2(111).

In all interface cases, an electrostatic dipole correction[44,45] is applied (*a posteriori*) perpendicular to the interface. This is done to compensate for the computational artifact of electrostatic coupling between supercells, through the vacuum region, which may give rise to artificial polarization effects (ideally, the vacuum region should be infinite). In our cases, no symmetry conditions in the structures prevent the formation of a dipole perpendicular to the interface, e.g., by charge transfer across the interface. However, in all cases, we find very small dipole energy corrections, of order 9 mJ/m^2 or less. Finally, we stress that ionic relaxations in all cases are performed using forces corresponding to the total energy density functional used; i.e., we do not evaluate the GGA energies by static (ion) calculations of the structure obtained by ionic relaxation using forces derived from the LSDA density functional; this would be a bad approximation,[46] considering the differences in predicted equilibrium bond lengths, as will be discussed in Secs. II D and III B.

D. The bulk phases of ZrO_2 and Ni

In this section we report a test of the pseudopotential setup for bulk ZrO_2 and Ni. To assure complete convergence of bulk properties with respect to Brillouin zone sampling, we use a 13×13×13 Monkhorst–Pack grid for the Ni bulk calculations in the *minimal* unit cells for fcc and bcc (containing one atom each), corresponding to a sampling spacing of $\kappa_{\text{BZ}} = \sqrt[3]{V_{\text{BZ}}}/13 \sim 0.22$ Å^{-1}, where V_{BZ} is the volume Brillouin zone. Apart from this, we have used same calculational parameters as outlined in Sec. II B.

In Table I we show equilibrium lattice constants, structural energy differences, and magnetic moments for bulk Ni, as obtained from our pseudopotential calculations. These results are in agreement with those in a recent study[47] investigating the transferability of ultrasoft pseudopotentials for Ni, Fe, and Co. They also compare very well with experiment and with results obtained by all-electron DFT-based methods.[48,49]

TABLE I. Cubic lattice constants a_0, structural energy differences ΔE and magnetic moments μ for fcc and bcc Ni. Magnetic moments are for the ferromagnetic solution in each case.

Method	XC functional	a_0^{fcc} (Å)	a_0^{bcc} (Å)	ΔE(bcc–fcc) (eV/Ni)	μ^{fcc} (spin/Ni)	μ^{bcc} (spin/Ni)
US-PP (This work)	LSDA	3.44	2.73	0.108	0.63	0.43
US-PP (This work)	GGA	3.53	2.81	0.100	0.63	0.62
FLAPW[a]	GGA	3.53	2.80	0.10	0.60	0.52
LMTO-ASA[b]	LSDA	3.44	2.73	0.04	⋯	⋯
LMTO-ASA[b]	GGA	3.53	⋯	⋯	⋯	⋯
Experiment[c]		3.52	⋯	⋯	0.61	⋯

[a]Reference 48.
[b]Reference 49.
[c]Reference 76.

The lattice constants obtained using the LSDA are 3% smaller than those obtained with the GGA, the latter agreeing very closely with the experimental value. This is in accordance with the trend established in the literature.[38,49,50–52] The (bcc–fcc) structural energy difference and corresponding magnetizations are insensitive to the choice of exchange-correlation functional, except for the ferromagnetic bcc electronic structure, where the magnetization using the LSDA is significantly lower than the value obtained with the GGA; again we emphasize that pseudopotential generation and our valence calculations had identical approximations for the exchange-correlation effects.

We also tested our Zr and O pseudopotential setup for the low-pressure polymorphs of ZrO_2. Recently, Jomard *et al.*[53] surveyed the bulk properties of the best-known ZrO_2 polymorphs and we obtain very similar results. These tests are also in good agreement with our earlier LDA results,[20] obtained with a Troullier–Martins pseudopotential set.[54] All degrees of freedom are relaxed, i.e., unit cell size and shape, as well as intracell coordinates, consistent with the symmetry of each phase (c-ZrO_2: $Fm\bar{3}m$; t-ZrO_2: $P4_2/nmc$ and m-ZrO_2: $P2_1/c$). All calculational unit cells have 4 formula units (although smaller unit cells for c- and t-ZrO_2 may be chosen, containing only 1 and 2 formula units, respectively). This enhances k-point error cancellation, because our unit cell choices have maximum coincidence between ZrO_2 polymorphs. We use a 4×4×4 Monkhorst–Pack grid for all ZrO_2 bulk calculations, corresponding to a sampling spacing of $\kappa_{\text{BZ}} = \sqrt[3]{V_{\text{BZ}}}/4 \sim 0.3$ Å^{-1}.

In Table II, we show the predicted lattice constants of each ZrO_2 phase. The table shows that generally the GGA overestimates the volume of ZrO_2, but this overestimation is uniform, so that shapes (lattice constant *ratios*, intracell coordinates, etc.) are in excellent agreement with experiment. The LSDA yields the correct volume, if Zr-semicore states are included in the valence, otherwise the LSDA has a tendency to underestimate lattice constants; the LSDA performs less well than the GGA with respect to shapes, even if Zr-semicore states are included in the valence, but still the agreement with experiment is satisfactory. The most important effect of Zr-semicore states in ZrO_2 is a uniform rescal-

TABLE II. Calculated lattice constants (a,b,c) (Å) at $T=0$ K for cubic (c), tetragonal (t), and monoclinic (m) ZrO_2. All unit cells are the conventional fluorite and distorted fluorite cells containing 4 formula units. δ_O/c is the tetragonal distortion of O-columns in t-ZrO_2 and β is the angle between ($\mathbf{a}$,$\mathbf{c}$) in m-ZrO_2.

			c-ZrO_2	t-ZrO_2			m-ZrO_2			
	Pseudopotentials[a]		a	a	c/a	δ_O/c	a	b/a	c/a	β
LSDA	Zr_I	O_I	5.034	5.037	1.012	0.040	5.080	1.023	1.027	99.30°
	Zr_I	O_{II}	5.046	5.050	1.011	0.036	5.096	1.024	1.025	99.40°
	Zr_{II}	O_{II}	5.082	5.086	1.013	0.040	5.136	1.020	1.029	99.43°
GGA	Zr_I	O_I	5.118	5.120	1.020	0.047	5.186	1.014	1.031	99.70°
	Zr_I	O_{II}	5.127	5.133	1.026	0.049	5.205	1.012	1.030	99.88°
	Zr_{II}	O_{II}	5.164	5.167	1.025	0.051	5.235	1.012	1.034	99.64°
Experiment			5.085[b]	5.053[c]	1.025[c]	0.049[c]	5.149[d]	1.012[d]	1.032[d]	99.23°

[a]O_I and O_{II} are soft and hard O pseudopotentials, respectively. Zr_I and Zr_{II} are pseudopotentials without and with Zr($4p$) semicore states in the valence, respectively.
[b]Reference 77, extrapolated to $T=0$ K using Ref. 79.
[c]Reference 78, extrapolated to $T=0$ K.
[d]Reference 79, extrapolated to $T=0$ K using the anisotropic thermal expansion coefficients $\boldsymbol{\gamma}=(1.03, 0.14, 1.47)\ 10^{-6}$/K from Ref. 80.

ing of volumes. Comparing results for pseudopotential set (Zr_I,O_I) with set (Zr_I,O_{II}) reveals marginal differences, i.e., O_I(soft) is just as transferable as O_{II}(hard) for the oxide. The only systematic effect is a marginal lattice contraction, less than 0.4%. The only systematic structural effect of Zr-semicore states in the valence is a uniform lattice expansion of order 1%; this brings the LSDA into very good agreement with experiment, but worsens the GGA overestimation of volume.

Table III shows that anion intracell coordinates are noticeably improved going from the LSDA to the GGA, whereas cation intracell coordinates are excellent in both cases. The residual errors in intracell coordinates, compared to experiment, do not improve upon including Zr-semicore states, nor do they depend on which O-pseudopotential (O_I or O_{II}) is used. We note that with respect to lattice constants, there is a fortunate error cancellation between on the one hand, the GGA volume overestimation, and on the other, omitting Zr-semicore states and, to a much lesser extent, using the soft O pseudopotential (O_I). Overall these error cancellations make the combination (Zr_I+O_I) best suited for the GGA from a structural point of view.

In Table IV we show the structural energy differences for ZrO_2 polymorphs. Generally the GGA overcorrects the LSDA underestimation of experimental structural energy differences. This was also noted in our previous work on the $ZrO_2(001)/\alpha$-$Al_2O_3(1\bar{1}02)$ interface,[18] using the so-called PB parameterization[35,55,56] of the GGA. As with structural properties, we find that O_I(soft) is just as transferable as O_{II}(hard) for relative energetics.

Our results in Table II–IV quantify the importance of Zr-semicore states for ZrO_2 [pseudopotential set (Zr_{II},O_I) vs (Zr_I,O_I)], in comparison with other approximations (e.g., the exchange-correlation functional and the pseudopotential ansatz). For the LSDA, it reduces the slight tendency to underestimate volume and provides moderate improvements in structural energy differences; in conjunction with the GGA,

TABLE III. Calculated intracell coordinates (with cell axes as the coordinate basis) at $T=0$ K, for structural generators of m-ZrO_2 in the conventional unit cell with 4 formula units. No ions occupy any special Wyckoff positions.

			Zr			O^1			O^2		
	Pseudopotentials[a]		x	y	z	x	y	z	x	y	z
LSDA	Zr_I	O_I	0.2776	0.0421	0.2097	0.0781	0.3509	0.3288	0.4467	0.7596	0.4833
	Zr_I	O_{II}	0.2782	0.0423	0.2091	0.0793	0.3533	0.3270	0.4464	0.7598	0.4843
	Zr_{II}	O_{II}	0.2783	0.0419	0.2095	0.0755	0.3461	0.3338	0.4472	0.7586	0.48
GGA	Zr_I	O_I	0.2766	0.0432	0.2094	0.0714	0.3380	0.3396	0.4489	0.7584	0.4797
	Zr_I	O_{II}	0.2771	0.0437	0.2090	0.0703	0.3361	0.3414	0.4490	0.7580	0.4801
	Zr_{II}	O_{II}	0.2768	0.0429	0.2097	0.0690	0.3334	0.3449	0.4501	0.7573	0.4783
	Experiment[b]		0.2754	0.0395	0.2083	0.0700	0.3317	0.3447	0.4496	0.7569	0.4792

[a]O_I and O_{II} are soft and hard O pseudopotentials, respectively. Zr_I and Zr_{II} are pseudopotentials without and with Zr($4p$) semicore states in the valence, respectively.
[b]Reference 79 (at 295 K).

TABLE IV. Structural energy differences (meV/formula unit) for the ZrO_2 polymorphs.

Pseudopotentials		$E^{c\text{-}ZrO_2}-E^{t\text{-}ZrO_2}$				$E^{t\text{-}ZrO_2}-E^{m\text{-}ZrO_2}$		
		LSDA	GGA	Exp[a]	Hartree–Fock[b]	LSDA	GGA	Exp[a]
Zr_I	O_I	39	75			40	105	
Zr_I	O_{II}	28	63	57	199	41	109	63
Zr_{II}	O_{II}	36	80			47	107	

[a]Reference 81.
[b]Reference 82.

it amplifies the disagreement with experiment, although it is formally a better approximation. The effect of Zr-semicore states in ZrO_2 is comparable to the sensitivity of exchange-correlation functional- and pseudopotential-parameterization (cf. Jomard *et al.*[53] for analysis of property sensitivity to particular GGA functional parameterizations). This conclusion is in partial disagreement with the claims of Jomard *et al.*[53] and Stapper *et al.*[57] (the latter authors only considered the LDA, though) that inclusion of Zr-semicore states in the valence is paramount for a reliable description of ZrO_2. At variance with Jomard *et al.*,[53] we draw the overall conclusion that GGA presents no significant improvement compared to the LSDA with respect to ZrO_2 bulk phases; nonetheless we prefer the GGA for the interface situation, which represents a more inhomogeneous chemical environment; here we expect GGA to perform better, similarly to adsorption energies, which are improved markedly with the GGA over the LSDA.[58] Furthermore, generally oxide surface energies seem to be predicted more realistically using the GGA, whereas the LSDA seems to overestimate this property for oxides.[59] In the rest of this paper, we will put emphasis on the GGA for exchange-correlation, although we will also present a few interface results obtained with the LSDA for comparison. As the pseudopotential pair (Zr_I, O_I) has the (unjustly) added advantage of reducing the GGA tendency to overestimate volume and further performs equally well with respect to energetics, we use (Zr_I, O_I) in the rest of this paper. This is of importance indirectly, since the GGA does *not* overestimate volume for Ni, and would consequently create artificial strain/strain release at the ZrO_2/Ni interface if the volume of ZrO_2 was incorrectly represented.

III. THE *c*-ZrO_2(111)/Ni(111) INTERFACE

A. Structural models for the ZrO_2/Ni(111) interface

Heterogeneous interface modeling has a crystalline and an atomistic aspect. The crystalline component is about matching lattice constants in two directions. The atomistic view is concerned with the detailed chemical and physical structure of the interface. The crystalline aspect is relatively simple to approach: one may write down a variety of simple models[1,60] that provide qualified guesses as to which faces of unequal crystals match well to one another. Obviously, the outcomes of such simple models need critical evaluation. For instance, one may match arbitrary crystal faces arbitrarily well to each other, if one assumes sufficiently large unit cells for both crystal surfaces comprising the interface. Similarly, excellent matchings for rather exotic Miller indices are produced for large interface unit cells.

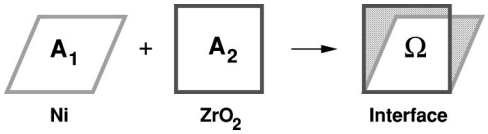

FIG. 1. Sketch of a surface unit cell of Ni with area A_1 and a surface unit cell of ZrO_2 with area A_2. Both unit cells may be multiples of the primitive surface unit cell, so that they contain several equivalent lattice points. Ω is the overlap area between the cells when overlaid.

In this study, we will apply a simple geometric model to survey the geometric aspect of matching ZrO_2 to a fcc Ni substrate. The model is illustrated in Fig. 1: some surface unit cell of ZrO_2 with area A_2 is forced into registry with a substrate Ni(fcc) surface unit cell, with area A_1. By overlaying these unit cells, as indicated on the right-hand side of Fig. 1, we calculate the overlap area Ω. We then define a misfit μ as

$$\mu = 1 - \frac{2\Omega}{A_1 + A_2}. \tag{2}$$

The measure μ is positive definite and quantifies the relative average length scale misfit (and not area mismatch) between two unit cells, which is seen by first order expansion in the shape difference between two unit cells. In Table V we show the best matching unit cell pairs, according to their μ-value, for cells with areas less than ~ 50 Å^2. We exclude some very elongated unit cells, which are rather unrealistic as interface unit cells.

TABLE V. Best matching supercells, according to the misfit measure μ defined in Eq. (2), of different Ni and *c*-ZrO_2 surfaces (restricted to surface supercell areas $\lesssim 50$ Å^2).

Crystal faces		Supercell	Misfit
Ni	*c*-ZrO_2	area (Å^2)	μ
100	100	12	0.026
100	110	37	0.029
100	111	43	0.035
110	110	17	0.026
110	100	26	0.007
110	100	26	0.029
110	111	35	0.053
110	111	44	0.016
111	111	37	0.051
111	111	48	0.032
111	100	53	0.045
111	110	59	0.035

We are interested in the adhesion of ZrO_2 deposited on a Ni-rich substrate. Given that the actual thermal barrier coating consists of zirconia doped with a few percent of a cubic oxide in order to stabilize cubic (c) and tetragonal (t) ZrO_2 over the entire temperature range of interest, we focus here on lattice matchings for c-ZrO_2 for simplicity (t-ZrO_2 will have essentially the same lattice misfit as the cubic phase in the lateral directions). The most abundant surface of fcc metals is the (111) facet, therefore we concentrate on matchings involving Ni(111), although the ZrO_2/Ni system offers several other (geometrically) very well-matched combinations involving other facets, e.g., c-$ZrO_2(100)$/Ni(110), as seen in Table V. Experimentally, it is often observed that an interface is preferred energetically between the most stable surfaces. Therefore the $ZrO_2(111)$/Ni(111) facet combination is likely to be relevant, as each facet is most stable for either material. [We have actually previously proposed[20] that m-$ZrO_2(\bar{1}11)$ is most stable. But $[\bar{1}11]$ and $[111]$ are equivalent by symmetry for c- and t-ZrO_2.]

Intuitively, one may speculate that more open surfaces would form stronger interfaces, as there are more ''dangling bonds'' available to form strong covalent bonds across an interface. However, the equilibrium state is determined by the interface tension,

$$\sigma_{A|B}=\sigma_{0|A}+\sigma_{0|B}-w_{A|B}, \tag{3}$$

where $w_{A|B}$ is the work of adhesion between facets A and B with surface tensions $\sigma_{0|A}$ and $\sigma_{0|B}$, respectively. As more open surfaces notoriously have higher surface tensions, it is the relative strength of interface vs bulk bonds that is decisive for whether the interface is preferred between open or compact surfaces. This competition between terms in Eq. (3) may be explored in a simple continuum model for the problem, which is linear in coordination changes. If we denote the coordination z of ions in the most compact surface and in the bulk as z^0 and z^b, respectively, and introduce the excess openness $x=(z^0-z)/(z^b-z^0)>0$ of a surface facet (i.e., the relative openness of a surface facet, compared to the most compact surface facet), we obtain

$$\sigma_{A|B}(x_A,x_B)=\sigma^0_{A|B}+x_A\left(\sigma^0_{0|A}-\frac{w^0_{A|B}}{2}\right)+x_B\left(\sigma^0_{0|B}-\frac{w^0_{A|B}}{2}\right), \tag{4}$$

where the superscript 0 refers to quantities pertaining to most compact facets A and B of each material. In deriving this equation, it is assumed that the interface coordination is proportional to $\sqrt{(z^b_A-z_A)(z^b_B-z_B)}$, i.e., the geometric average of the ''missing'' surface coordination. Equation (4) indicates that the interface is more stable between less-compact surfaces, if $2\sigma^0_{0|A}<w^0_{A|B}$ and/or $2\sigma^0_{0|B}<w^0_{A|B}$. This confirms the statement above that it is the relative strength of interface versus bulk bonds for either material that is decisive for whether an open or compact surface facet of either material will be present at a stable interface. Of course, the estimate of Eq. (4) is a very crude one.

We have chosen the c-$ZrO_2(111)$/Ni(111) combination in Table V, with the smaller (and computationally manageable) unit cell. A mismatch of 5% still makes epitaxial growth possible. A top view of these surface unit cells of Ni(111) and c-$ZrO_2(111)$ is sketched in Fig. 2. They correspond to Ni(111) $\sqrt{7}\times\sqrt{7}$ and c-$ZrO_2(111)$ $\sqrt{3}\times\sqrt{3}$ in terms of primitive surface unit cells. The interface unit cell axes are 6.6×6.6 Å.

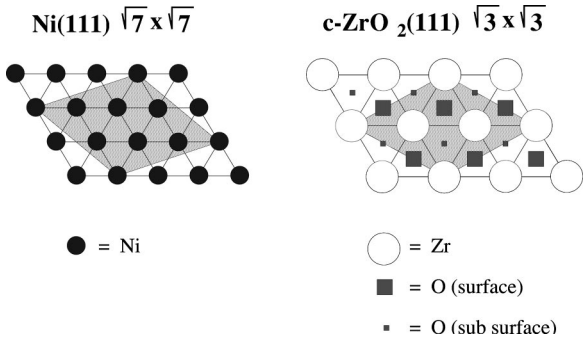

FIG. 2. Top view of the first layer of Ni(111) and c-$ZrO_2(111)$. The matching unit cells are gray toned.

We note that this cell choice does not rigorously support phase transitions to t-ZrO_2 or m-ZrO_2; this would require a surface unit cell double this size. In Sec. III B, we will see that the ZrO_2 overlayers undergo a partial ''local'' phase transition to m-ZrO_2, despite the constraint imposed by the periodic boundary conditions. Which phase ZrO_2 attains (locally) is less important for the local interface cohesion per se; the energy associated with oxygen ions performing the tetragonal distortion is of order 40 meV/oxygen, compared to interface metal–oxygen bonds >0.5 eV, as we will discuss in Sec. III C. On a macroscopic scale, however, ZrO_2 phase transitions (induced by thermal cycling) are of paramount importance for the work of adhesion, as they lead to stress build-up, defect formation, and finally spallation of ZrO_2. Our calculations are restricted to ideal interfaces.

The atomistic features of heterogeneous interfaces are more complex than the lattice matching aspect discussed above. The stoichiometry of the interface depends, in addition to the energetics, on the actual chemical potentials (including those of impurities) as well as kinetic limitations. We limit this study to the case of stoichiometric ZrO_2 deposited on Ni(111), because it is currently computationally prohibitive to realistically model off-stoichiometric effects by first principles calculations. This poses a restriction on the comparison of our results with real-life Ni/ZrO_2 interfaces, where either excess Zr or O might be present during film growth, e.g., via vapor deposition, as it is well known that partial pressures can have significant influence on the interface atomic morphology. The surface termination of Ni(111) is quite unambiguous and well established. c-$ZrO_2(111)$ has a stacking sequence like $\cdots|O|Zr|O|O|Zr|O|O|Zr|O|\cdots$ [this also pertains to t-$ZrO_2(111)$, but here the O-layers are rumpled; for m-$ZrO_2(\bar{1}11)$ and m-$ZrO_2(111)$, the stacking may also be considered to be $\cdots|O|Zr|O|O|Zr|O|O|Zr|O|\cdots$, but all layers are rather rumpled; see figures in Christensen and Carter[20]]. Therefore, it is most natural to consider a $ZrO_2(111)$ layer as $|O|Zr|O|$, which we will do for the rest of this paper. A schematic top view of this layer is shown in Fig. 2.

The structural models used for extended interfaces fall

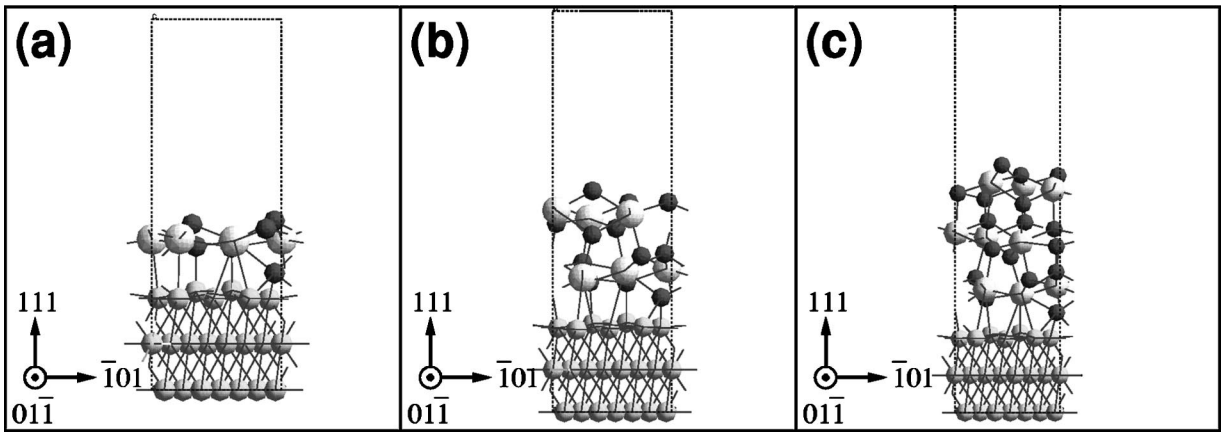

FIG. 3. Side view of one (a), two (b), and three (c) layers of $ZrO_2(111)$ adsorbed onto a Ni(111) substrate in the Ni(111)$\sqrt{7}\times\sqrt{7}$ interface unit cell. All ions, except the two lowest Ni(111) layers (away from the interface) are relaxed. Ni ions are gray and small; Zr ions are white and large; O ions are dark and small. The directional arrows refer to the substrate.

into two main categories: cluster and slab models. While cluster models may support very accurate quantum chemical calculations, they suffer from edge effects. Unfortunately, convergence of many electronic properties with cluster size is rather slow so that intractably large clusters are necessary to get a realistic representation of the extended interface. Slab models on the other hand enforce some periodicity in the interface plane, so that edge atoms have a more realistic environment. Slab models also reproduce dispersion of electronic states, being infinite parallel to the surface. As a drawback, the enforced periodicity may induce artificial strain. The strain may systematically be reduced by enlarging the interface unit cell, but quickly the calculations become computationally intractable.

We use the supercell approach, where slabs are repeated perpendicular to the interface and separated by vacuum, i.e., the physical interface is modeled by a sequence like $\cdots|\mathrm{Ni}|\mathrm{ZrO_2}|\mathrm{vacuum}|\mathrm{Ni}|\mathrm{ZrO_2}|\mathrm{vacuum}|\mathrm{Ni}\cdots$. The vacuum region is 10 Å thick, which is empirically sufficient to ensure vanishing wave function overlap across the vacuum region;[20] long-ranged electrostatic coupling across the vacuum region is compensated by means of an electrostatic dipole correction.[44,45] The Ni-segment must be thick enough that Ni-surface/interface coupling through the Ni-segment is negligible, to model an infinite Ni-substrate. We use a three-layer Ni(111) slab and we justify in Secs. III B and III C that this is sufficient to reliably model an infinite Ni-substrate. For high symmetry epitaxial interfaces, like Ag(100)$\|$MgO(100),[61] the vacuum region may sometimes be omitted. However, the symmetry of $ZrO_2(111)$/Ni(111) is too low for this. Our primary motivation for this study was to model TBC's, where the thermal insulating ceramic is deposited onto the substrate metal. Therefore we let the Ni(111) substrate unit cell determine the interface lattice constant, which is held fixed to the theoretical value for bulk Ni (corresponding to the particular exchange-correlation functional used).

B. Interface structure

In Fig. 3 we show a side view of 1, 2, and 3 layers of $ZrO_2(111)$ adsorbed onto a Ni(111) substrate in the Ni(111) $\sqrt{7}\times\sqrt{7}$ interface unit cell. All ions, except the two lowest Ni(111) layers (away from the interface) are relaxed to their equilibrium positions. We wish to emphasize that local minima exist on the interface configuration potential energy surface (PES). We started the ionic relaxation with the ceramic layer translated by different, arbitrary vectors parallel to the substrate, and in some cases, the ionic relaxation found a local minimum; this represents an added difficulty in the study of complex interface structures. We only present results corresponding to the most stable equilibrium interface found. The interface structure does not appear to be very dependent on the thickness of the ceramic layer. This suggests that the interface structure may be explored in larger detail by a local model, involving only ions in the vicinity of the interface. However, indirect elastic effects may come into play for thicker ceramic layers.

The $ZrO_2(111)$ overlayers maintain a $\cdots|\mathrm{O}|\mathrm{Zr}|\mathrm{O}|\mathrm{O}|\mathrm{Zr}|\mathrm{O}|\mathrm{O}|\mathrm{Zr}|\mathrm{O}|\cdots$ type stacking, which offers the lowest electrostatic energy, but appears somewhat glassy. The slab with 3 layers of $ZrO_2(111)$ [Fig. 3(c)] has transformed partially to m-ZrO_2, as seen from the characteristic sevenfold coordination of cations and alternating three and fourfold coordination of anions in the middle of the ceramic film. This is not surprising, m-ZrO_2 being the most stable

TABLE VI. Typical coordination across the interface in the Ni(111)$\sqrt{7}\times\sqrt{7}$ interface unit cell. Ion superscripts refer to the coordination number across the interface. This qualitative coordination pattern is independent of the number of ceramic layers.

Abundance/unit cell	Ion	→	Neighbor(s)	Comments
	Viewed from ZrO_2 side			
2	Zr^1	→	Ni	
1	Zr^2	→	Ni, Ni	one short, one longer bond
2	O^1	→	Ni	tilted on-top
1	O^3	→	Ni, Ni, Ni	pseudo hollow site
	Viewed from Ni side			
2	Ni^{1a}	→	Zr	
3	Ni^{1b}	→	O	
2	Ni^2	→	Zr,O	

TABLE VII. Adiabatic works of adhesion $w_{ZrO_2\|Ni}$(mJ/m^2), average bond lengths (Å) across the interface in the Ni(111) $\sqrt{7}\times\sqrt{7}$ interface unit cell, sorted according to bond types (see Table VI), and average dilation (Å) (along the interface normal) of the topmost Ni(111) layer, when ZrO_2 layers are adsorbed, together with the standard deviation in the dilation.

Ni(111) layers	3	3	3	4	3
ZrO_2 layers	1	2	3	1	1
XC-functional	GGA	GGA	GGA	GGA	LSDA
Work of adhesion $w_{ZrO_2\|Ni}$	2011	1308	995	1969	2749
Bond lengths for bond type:					
$Zr^1 \rightarrow$ Ni	2.66	2.93	2.88	2.66	2.59
$Zr^2 \rightarrow$ Ni, Ni	2.86	2.72	2.78	2.86	2.77
$O^1 \rightarrow$ Ni	1.97	2.02	2.04	1.98	1.93
$O^3 \rightarrow$ Ni, Ni, Ni	1.90	2.08	2.02	1.91	1.85
Interface Ni layer corrugation					
Average dilation	0.051	0.030	0.032	0.054	0.030
Standard deviation	0.15	0.11	0.12	0.15	0.13

polymorph. However, the ceramic film is not able to transform completely to m-ZrO_2, due to the constraints imposed by the periodic boundary conditions, which create geometric frustration. Another indirect driving force for $(c\rightarrow m)$-ZrO_2 transition is the tensile stress associated with c-$ZrO_2(111)$ being expanded by 5%, imposed by the periodic boundary conditions. Since the volume of m-ZrO_2 is 7% larger than c-ZrO_2 (at $T=0$ K), the transformation reduces the misfit in the ceramic layer to less than the 5% shown for the c-$ZrO_2(111)\|Ni(111)$ match in Table V. A crude estimate indicates an actual compressive strain of order 2% in the ceramic overlayer due to the pseudo m-ZrO_2 structure that is formed. Thus, this interface reduces the strain by converting 5% tensile stress to 2% compressive strain via conversion of cubic to monoclinic ZrO_2. Whether this would occur at an interface with less tensile stress, modeled within a supercell, is an open question. At the moment, this is beyond our computational means to consider.

The coordination pattern of ions closest to the interface plane is quite similar for either 1, 2, or 3 layers of ZrO_2 adsorbed. There are typically 9 interface bonds per unit cell. This is detailed in Table VI. This table shows which kind of neighbors an ion typically has on the opposite site of the interface. The Ni–O bonds are the most important: surface anions on the ZrO_2 side touch the Ni(111) surface in hollow sites and on-top sites in the ratio 1/2. One might speculate that it is energetically preferred to maximize the number of anions being in hollow sites, as the hollow site is preferred over the on-top site by ~1 eV/oxygen (Ref. 62) for O/Ni(111) (neutral oxygen atoms). However, due to the intrinsic length scale misfit, the interface must accept some less favorable Ni–O bonds to obtain some favorable Ni–O bonds.

The slab with 2 layers of ZrO_2 [Fig. 3(b)] deviates a little from the pattern; the hollow site anion sits rather asymmetrically, so that this configuration is in between a bridge and hollow site situation. This is most likely an indirect effect induced by the upper ZrO_2 layer. Zr ions coordinate weakly with Ni atoms via what may be considered as diffuse (long) bonds. Per $\sqrt{7}\times\sqrt{7}$ unit cell, two Zr ions each coordinate with one Ni atom, while another Zr ion coordinates with two Ni atoms across the interface.

In Table VII we display the average bond lengths across the interface according to bond type and model parameters. The interface bond lengths are converged to an asymptotic value already at 2 layers of ZrO_2. Interface bond lengths for a single layer of ZrO_2 are much shorter, indicating that a single ceramic layer bonds strongest to the metal substrate. As usual, the interface bonds are predicted to be longer when using the GGA compared to the LSDA; the ratio corresponds approximately to that seen for bulk ZrO_2 lattice constants in Table II. The table shows that Ni–Zr interface bond lengths are 2.7–2.9 Å (within the GGA). The average bond length for bulk metallic Ni and Zr is 2.76 Å, suggesting that the Ni–Zr interaction at the interface is weak, but present. Comparing the results for 3 and 4 layer Ni substrates in Table VII suggests that the interface structure is fairly converged with respect to substrate thickness; in other words, the 3-layer Ni slab is a reasonable model for the infinite Ni substrate from a structural point of view. We note that the results in Table VII are slightly influenced by the constraints imposed on the lower Ni-substrate layers. This most likely corresponds to a small rescaling of the rumpling in the Ni-interface plane.

Figures 3(a)–3(c) illustrates that the onefold interface anions (labeled O^1 in Table VI) drag out Ni atoms slightly from the Ni-substrate. Adsorbed oxygen in related situations have been observed to pull metal substrate atoms outwards. For PdO(001)/Pd(100), a surface corrugation of Pd(100) of order 0.26–0.51 Å was observed by tensor LEED analysis.[63] For reconstructed O/Cu(100), LEED indicates vertical relaxations of order 0.10 Å.[64] For Fe(001)-(1×1)O [which may be considered as a monolayer of FeO onto Fe(001)], a smaller outward relaxation of 0.01 Å for the first clean Fe(001) layer was deduced by Auger spectroscopy and medium-energy ion scattering.[65] In Table VII, we show the structural perturbation of the Ni(111) substrate by forming the interface. The dilation of the topmost Ni(111) is referenced to the unrelaxed bulk termination [keeping in mind that the surface relaxation for Ni(111) is minute[66]]. The standard deviation in the position distribution of interface Ni atoms gives a quantitative estimate of the ceramic-induced corrugation of the Ni substrate. The standard deviation is larger than the average position along the interface normal, because 2 interface Ni atoms in the supercell are dragged rather far out of the substrate (0.17–0.32 Å), whereas the remaining 5 interface Ni atoms in the supercell are repelled weakly by the ceramic (by around 0.04 Å). Table VII also supports the picture that a single layer bonds strongly (and perturbs the substrate most), whereas the bonding loosens and saturates for two or more ceramic layers. The fact that the LSDA predicts 40% less dilation than the GGA is striking (compared to previous differences in lattice constants of order 2%), but possibly may be attributed to the relative smallness of the dilation, compared to the magnitude of bond lengths. Again we notice, by comparing the results for 3 and 4 layer Ni substrate in Table VII that results are well converged with respect to substrate thickness.

C. Interface cohesion

In this section we focus on the energetic aspects of the ZrO_2(111)/Ni(111) interface. The main quantity is the adiabatic work of adhesion $w_{ZrO_2\|Ni}>0$,

$$w^N_{ZrO_2\|Ni}=\frac{E_{0\|Ni}+(E^N_{0\|ZrO_2}-E^N_{ZrO_2\|Ni})}{A}, \quad (5)$$

where $E_{0\|Ni}$ and $E_{0\|ZrO_2}$ refer to the total energies of the relaxed, isolated Ni and ZrO_2 films, respectively, and $E_{ZrO_2\|Ni}$ refers to the total energy of the relaxed interface structure. A is the interface area of the unit cell and N is the number of ceramic layers. Generally, the mechanical work $w^{mech}_{ZrO_2\|Ni}$ needed to physically separate an interface is larger than the adiabatic work of adhesion $w_{ZrO_2\|Ni}$ due to dissipative processes, as discussed by Finnis.[67] Thus our predictions may be considered as lower bounds for the work of adhesion obtained by any cleavage experiment.

In Eq. (5), we use values for $E_{0\|ZrO_2}$ corresponding isolated ZrO_2 films stretched slightly (transversally) to accommodate the Ni substrate, corresponding to the Ni(111) $\sqrt{7}\times\sqrt{7}\,\|\,c$-$ZrO_2$(111) $\sqrt{3}\times\sqrt{3}$ match (but allowing the ceramic film to relax fully perpendicular to the interface). We use this convention, because otherwise $w_{ZrO_2\|Ni}$ contains a bulk elastic component, which diverges with increasing numbers of ZrO_2 layers (N) deposited. This bulk strain component is unrelated to the local cohesive properties of the interface per se, which we want to characterize. The convention of using $E_{0\|ZrO_2}$ for the stretched state is also sensible for the following reason: the real life interface has defects on the ZrO_2-side to release stresses; these crystal defects persist long after the physical separation of the interface, on a time scale of the separation process. Therefore the ZrO_2 crystal defect energy should tend to cancel between $E_{0\|ZrO_2}$ and $E_{ZrO_2\|Ni}$ in Eq. (5), if a realistic interface model is used. Likewise the strain energy component, induced by the need of PBC in our calculations, cancels between $E_{0\|ZrO_2}$ and $E_{ZrO_2\|Ni}$ in Eq. (5) when the ZrO_2 is in the strained state, so that this energy *difference* $E_{0\|ZrO_2}-E_{ZrO_2\|Ni}$ is realistically predicted, even though the model systems $0\|ZrO_2$ and $ZrO_2\|Ni$ both are in a strained state. This error cancellation lessens the severity of the epitaxial assumption inherent for the PBC. This cancellation principle may also be applied to *differences* in structural aspects, induced by interface formation, although the argument is somewhat weaker in this respect.

It is possible to conceive a second adiabatic work of adhesion $u_{ZrO_2\|Ni}$, which covers processes on all time scales,

$$u_{ZrO_2\|Ni}=\frac{E_{0\|Ni}+E_{0\|ZrO_2(\infty)}-E_{ZrO_2\|Ni}}{A}, \quad (6)$$

where $ZrO_2(\infty)$ symbolizes a complete structural equilibrium of the isolated ZrO_2 film. Then, generally, the following inequality will hold: $u_{ZrO_2\|Ni}<w_{ZrO_2\|Ni}<w^{mech}_{ZrO_2\|Ni}$. It is $w_{ZrO_2\|Ni}$ that is important for the mechanical properties of the interface. The energy difference $(w_{ZrO_2\|Ni}-u_{ZrO_2\|Ni})$ is dissipated after the interface separation.

In Table VII we show adiabatic work of adhesion $w_{ZrO_2\|Ni}$, calculated as discussed above. It is seen that the bonding of a single ceramic layer is relatively strong, of order 2000 mJ/m^2, using the GGA. The bonding is significantly decreased, when the thickness of the ceramic layer is increased. This is in accordance with the trend in interface bond lengths discussed in Sec. III B. The asymptotic level (corresponding to a useful TBC) is less than 1000 mJ/m^2. Extrapolating $w^N_{ZrO_2\|Ni}$ to a macroscopically thick ceramic film ($N=\infty$) using the two parameter form,

$$w^N_{ZrO_2\|Ni}=w^\infty_{ZrO_2\|Ni}+(w^1_{ZrO_2\|Ni}-w^\infty_{ZrO_2\|Ni})\exp\frac{N-1}{\lambda} \quad (7)$$

gives $w^\infty_{ZrO_2\|Ni}=745$ mJ/m^2 and $\lambda=1.2$ layers. The decay of $w^N_{ZrO_2\|Ni}$ with N is slower than for our recent study of the $ZrO_2(001)/\alpha$-$Al_2O_3(1\bar{1}02)$ interface, where $w^N_{ZrO_2\|Al_2O_3}$ was essentially converged at $N=1$. Results in Table VII are obtained by subtracting energies of structures in similar unit cells, to achieve maximum error cancellation with respect to k-point sampling. Interslab dipole corrections are applied to all results also, but the magnitude of the dipole interaction energy was found to be very small in all cases, of order 9 mJ/m^2, for the vacuum layer thickness (10 Å) applied in our calculations. We note from Table VII that the cohesive energies are fairly converged with respect to substrate thickness, so that they are much less sensitive to substrate thickness than the ceramic film thickness; this is probably due to the fact that the screening is more efficient in the Ni metal substrate than in the ceramic.

Our observation that a single ceramic layer bonds strongly, whereas the bonding is weakened for many ceramic layers is a mirror of the trend noticed for metals deposited onto ceramics; many metals are predicted to wet, but then ball up for more than one monolayer deposited,[46,68,69] i.e., growing in a Stranski–Krastanov fashion. Note that the trend that the ceramic favors interceramic bonds when the thickness of the ceramic layer is increased is opposite of that expected from the simplest image charge interaction model,[67] which states that the major contribution to metal–ceramic bonding is the electrostatic attraction between the ceramic and its (oppositely-charged) image in the metal: a thicker ceramic layer would produce a larger (oppositely charged) electrostatic image in the metal and thus bond stronger. The reason the image charge model breaks down is that the cohesion changes character (becomes more covalent) for very thin ZrO_2 films. We will discuss this in more detail in Sec. III D.

As expected, the LSDA value for $w_{ZrO_2\|Ni}$ is significantly larger than the corresponding GGA value. Interestingly, it is 37% larger, whereas the cohesive energies for bulk ZrO_2 and Ni are ''only'' 10%–20% larger with the LSDA compared to the GGA. This shows that differences between the LSDA and GGA predictions are nonhomogeneous.

Averaging the cohesive energy obtained with the GGA over interface bonds gives an average bond strength of 0.52 eV/bond for a single ceramic layer, decreasing to 0.2 eV/bond for an infinitely thick ceramic layer. The corresponding LSDA value is 0.68 eV/bond for a single ceramic layer. These values are based on 9 interface bonds per unit cell, i.e., both the short Ni–O and diffuse Ni–Zr bonds are counted on an equal footing.

The fact that the ZrO_2/Ni interface is weakly bonded also emerges from the interface tension, Eq. (3),

$$\sigma_{ZrO_2\|Ni} = \sigma_{0\|Ni} + \sigma_{0\|ZrO_2} - w_{ZrO_2\|Ni}. \tag{8}$$

For a nonstoichiometric interface, Eq. (8) would involve chemical potentials as well. The sign and magnitude of $\sigma_{ZrO_2\|Ni}$ tells whether the interface bonds are stronger than the internal bonds in each ceramic, so that $0 < \sigma_{ZrO_2\|Ni} < \sigma_{0\|Ni} + \sigma_{0\|ZrO_2}$ corresponds to weakly coupled interfaces, and $\sigma_{ZrO_2\|Ni} < 0$ to strongly coupled interfaces. A very negative $\sigma_{ZrO_2\|Ni}$ may reflect a propensity to form an intermediate phase (chemically mixed) at the interface. The Ni and (transversally) stretched ZrO_2 films have asymptotic surface tensions of 1900 and 650 mJ/m^2, respectively (using the GGA density functional) implying $\sigma_{ZrO_2\|Ni} \sim$ 1800 mJ/m^2 for an infinitely thick ceramic film; the sign and magnitude of $\sigma_{ZrO_2\|Ni}$ does not change for a single ceramic layer (the surface energy of a single ceramic layer is larger than for a thick ceramic film). These values are consistent with the limited body of experimental data available. Duh and Chien[70] and also Wang *et al.*[71] found no interphase formation (interfacial reaction) between Ni and ZrO_2 under clean conditions, consistent with $\sigma_{ZrO_2\|Ni} > 0$. Tsoga, Naoumidis, and Nikolopoulos[72] found no (macroscopic) wettability of Ni on YSZ in sessile drop experiments and observed a contact angle of $\theta = 117°$. The Young equation for the contact angle of θ relates the surface tension and adhesive work for this case as

$$\cos(\theta) = \frac{\sigma_{0\|Ni} - \sigma_{ZrO_2\|Ni}}{\sigma_{0\|ZrO_2}} = \frac{w_{ZrO_2\|Ni}}{\sigma_{0\|ZrO_2}} - 1. \tag{9}$$

This points to an even smaller value of order $w_{ZrO_2\|Ni} \sim$ 350 mJ/m^2 (using our extrapolated GGA value for $\sigma_{0\|ZrO_2} = 650$ mJ/m^2). This is easily rationalized, because their experiment used YSZ as opposed to the stoichiometric, pseudocrystalline ZrO_2 in our calculations. Furthermore, our results apply to an ideal interface with 100% contact area. The results of Duh and Chien[70] indicate that a contact area of 30%–70% is more common in the Ni/YSZ interface system. Therefore the situation is fully rationalized by accordingly scaling down our ideal value of $w_{ZrO_2\|Ni}$.

One may worry that the weak interface bonding we find is an artifact due to the strain induced by the periodic boundary conditions, imposed for methodological reasons in our calculation. However, since the strain is primarily tensile, this would act oppositely; a bond stretching in the ceramic layer is more likely to induce an interface bond strengthening. Therefore we find it unlikely that an imaginary calculation without imposed periodic boundary conditions would lead to increased interface cohesion. Further, the ceramic system releases the tensile stress by transformation to a pseudo m-ZrO_2 phase. In other recent work,[18] we found that thin c-$ZrO_2(001)$ films transformed to m-$ZrO_2(001)$, even without an imposed strain in the ceramic layer.

One may also speculate that c-$ZrO_2(111)$/t-$ZrO_2(111)$ offers better steric possibilities for matching Ni(111), as compared to m-$ZrO_2(111)$/m-$ZrO_2(\bar{1}11)$, but that this is suppressed because an artificial PBC induced strain dominates energetically. This cannot be excluded *a priori*, but we note that either ZrO_2 polymorph has a similar (111) stacking sequence, $\cdots|O|Zr|O|\cdots$, and the surface anion lattice forms a (distorted) hexagonal structure in all cases, to minimize electrostatic repulsion. This fact renders the latter possibility less likely.

TABLE VIII. Reference valence charge and magnetic moment (using the GGA) for isolated $ZrO_2(111)$ and Ni(111) films (3 layers each), as obtained by integrating atom-projected electronic DOS within spheres around each nucleus ($r_{Ni} = 1.372$ Å, $r_{Zr} = 1.630$ Å, and $r_O = 1.210$ Å). The ZrO_2-films are in the uniformly expanded state, to accommodate the Ni(111) lattice constant.

		Charge (electrons/ion)	Magnetic moment (μ_B/ion)
Bulk	Ni	9.52	0.71
	Zr	2.89	0
	O	6.42	0
Surface	Ni	9.36	0.68
	Zr	2.79	0
	O	6.29	0

D. Density of states at the interface

We carry out an electronic density of states (DOS) analysis by integrating the occupied, atom-projected DOS, obtained by projecting electronic states onto spherical harmonics inside spheres, centered at each ionic site. We use the radii $r_{Ni} = 1.372$ Å, $r_{Zr} = 1.630$ Å, and $r_O = 1.210$ Å. Similarly, local electronic spectral (e.g., local DOS) properties are obtained by projecting electronic Bloch states onto spherical harmonics centered inside the same spheres. These radii corresponds to volume-conserving (i.e., space-filling and weakly-overlapping) spheres at the equilibrium lattice constants for Ni(fcc) and c-ZrO_2. For ZrO_2, an additional constraint is necessary to fix the ratio r_O/r_{Zr}. The most obvious choice is to determine this from their respective ionic radii, i.e., $r_O/r_{Zr} = 1.30/0.84$. However, this leads to a value of r_{Zr} inside the pseudization radius for Zr; therefore we set $r_{Zr} \sim r_{ps}^{Zr}$ and determine r_O from the volume conserving requirement for c-ZrO_2 at the equilibrium lattice constant. For c-ZrO_2 at the equilibrium lattice constant for the GGA, this yields 2.80 and 6.48 valence electrons per Zr-ion and O-ion, respectively. It would be misleading to choose these radii so as to reproduce the nominal cationic/anionic electronic charges (0/8 electrons, respectively), since this implies $r_{Zr} = 0$. This procedure is nonunique and the results depend somewhat on choice of sphere radii, in that charge in (small) regions of space, where spheres overlap, are counted twice, whereas ''interstitial'' charge is not counted at all. The pro-

TABLE IX. Layer-averaged, angular-momentum-resolved DOS, local band center, and local band width for Ni atoms (using the GGA) for the interface configuration with 3 layers ZrO_2(111) deposited onto 3 layers Ni(111). See text for further details. Numbers are obtained by projecting electronic states onto atomic spheres with $r_{Ni} = 1.372$ Å. The energy zero point is set to the Fermi level. Totals (col. 4, 8, 12) refer to weighted averages, i.e., to the quantities obtained from DOS moments after angular momenta were summed out.

Ni type	DOS (electrons/Ni)				Occupied valence Local band center (eV)				Local band width (eV)			
	s	*p*	*d*	Total	*s*	*p*	*d*	Total	*s*	*p*	*d*	Total
Interface	0.52	0.52	8.44	9.48	−5.24	−3.81	−2.06	−2.31	2.73	2.95	1.36	1.76
Bulk	0.53	0.56	8.42	9.51	−5.37	−3.40	−2.20	−2.42	1.73	1.52	1.23	1.48
Surface	0.53	0.44	8.39	9.36	−4.36	−2.91	−1.91	−2.08	1.89	1.68	1.05	1.27

cedure does not strictly conserve charge, generally speaking. For instance, the charge in volume-filling spheres for Ni(fcc) is 9.52 electrons as opposed to the nominal 10 electrons. Similarly, for *c*-ZrO_2 (at the equilibrium lattice constant), only 15.75 electrons/ZrO_2, compared to the nominal 16 electrons/ZrO_2, are recovered by charge integration over spheres with the chosen radii. However, trends and charge differences are predicted more robustly when using a consistent set of projection sphere radii. No unambiguous method exists for attributing electronic properties to particular atoms, although some schemes, like Mulliken population analysis, have certain advantages.

In Table VIII we show absolute sphere charge and polarization for isolated Ni(111) and ZrO_2(111) obtained with this choice of sphere radii. The ZrO_2-films have pseudomonoclinic structures, as discussed in Sec. III B, and are in the (transversally) stretched state, to accommodate the Ni(111) lattice constant. In Table VIII, ''bulk'' refers to the middle film layer, which empirically has electronic properties very similar to the bulk (for materials like Ni and ZrO_2). The Zr ions labeled as ''surface'' in Table VIII do not protrude from the surface, but reside approximately 0.7 Å below the surface terminating anions. The surface ions lose 0.1–0.15 electrons; this is mainly a vacuum spill-out effect. We also find that the magnetic moment decreases 0.03 μ_B/Ni, going from Ni bulk to the surface Ni(111).

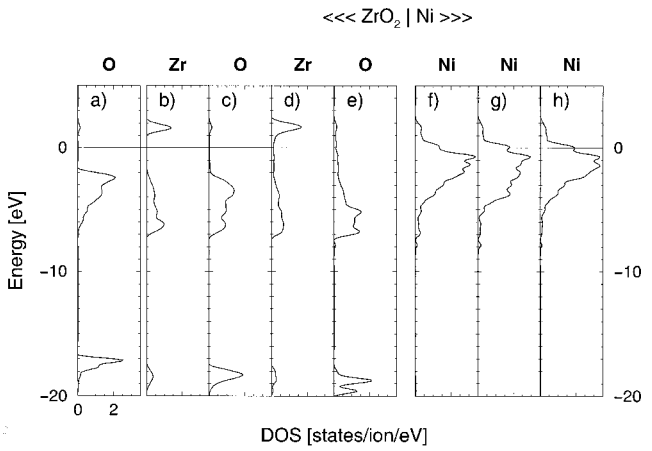

FIG. 4. Electronic density of states profile, averaged over ionic layers parallel to the interface, for the interface structure in Fig. 3(c) with 3 substrate layers Ni(111), and 3 layers ZrO_2(111). The energy zero is at the Fermi level. (a) ''Surfacelike'' O(111), from the 3rd ceramic layer. (b),(c) ''Bulklike'' Zr and O from the 2nd ceramic layer. (d),(e) Interface Zr and O, from the 1st ceramic layer. (f) Interface Ni, from the 1st substrate layer. (g) Bulklike Ni, from the 2nd substrate layer. (h) ''Surfacelike'' Ni(111), from the 3rd substrate layer.

In Table IX we have resolved the electronic DOS (using the GGA) for the three Ni substrate layers, which are surface-, bulk-, and interfacelike, respectively, to elucidate differences in chemical environments. The table shows the angular-momentum-resolved DOS (ρ_0), local band center (*c*) and local band width (*w*), which are generated conventionally from the first moments of the Ni local DOS $\rho_n^L = \int^{\epsilon_F} \epsilon^n \rho^L(\epsilon) d\epsilon$, ϵ_F being the Fermi energy and *L* the angular momentum quantum numbers. Explicitly, $c^L = \rho_1^L/\rho_0^L$, and $w^L = \sqrt{(\rho_2^L - (\rho_1^L)^2)/\rho_0^L}$. The angular-momentum-averaged quantities are formed similarly, using $\rho_n = \Sigma_L \rho_n^L$. These entries are labeled ''Total'' in Table IX. The layer averages displayed are tabulated as simple averages over corresponding ion-projected quantities. Most noticeable is that the bottom of the Ni valence region attains more *p*-character, by interaction with the ZrO_2 O(2*p*) valence band. Also, the interface band width is larger than the bulk value, indicating covalent Ni–O interactions.

Figure 4 shows the local DOS of the interface structure, where the graphs are arranged along the interface normal, to provide a spatial profile: ceramic surface → ceramic bulk → interface → Ni bulk → Ni surface. The energy zero is chosen at the Fermi level. The lowest feature on the oxygen ions, 17–19 eV below the Fermi level, is the narrow O(2*s*)-derived band with a band width around 1–2 eV, indicating the O(2*s*) electrons are very localized. The ceramic valence band is derived from the O(2*p*) states and shows a larger dispersion than the O(2*s*) band, indicating significant delocalization. The ceramic conduction bands are derived from the cation Zr(4*d*) valence states, with the bottom of the conduction bands being mainly *d*-like. The valence region of Ni is dominated by the *d*-band, the top of which is cut by the Fermi level. The bottom of the bulk Ni valence band has *s*-character.

Interface anions are noticeably perturbed by the formation of the interface: O(2*s*,2*p*) features are shifted down. This is due to the image potential set up by the Ni substrate, which screens the Madelung potential imposed by the ceramic. The image charge interaction is most likely the major component of the cohesion for this trilayer film. The O(2*s*) states are split up in two peaks; these correspond to two different kinds of oxygen (O^1, O^3, see Table VI) found at

TABLE X. Layer-averaged valence charge (electrons/ion) and magnetic moment (μ_B/ion) (using the GGA) for the interface configuration with 3 layers $ZrO_2(111)$ deposited onto 3 layers Ni(111). Layers are numbered in ascending order away from the interface. For induced charge/magnetic moment, the reference state is either corresponding ions in the isolated film or bulk ions.

Ceramic or metal layer	Ion type	Absolute		Induced (vs film)		Induced (vs bulk)	
		Charge	Moment	Charge	Moment	Charge	Moment
	O	6.43	0.00	0.00	0.00	0.00	0.00
2 (bulk)	Zr	2.88	0.00	−0.01	0.00	−0.01	0.00
	O	6.42	0.00	0.00	0.00	0.00	0.00
	O	6.41	0.00	−0.02	0.00	−0.02	0.00
1 (interface)	Zr	2.81	−0.04	0.01	−0.04	−0.08	−0.04
	O	6.42	0.04	0.13	0.04	0.00	0.04
			Interface				
1 (interface)	Ni	9.48	0.56	0.12	−0.12	−0.04	−0.16
2 (bulk)	Ni	9.51	0.67	−0.01	−0.04	−0.01	−0.04

the interface. The hollow site oxygen (O^3) is associated with the lowest energy peak. Some *p*-like DOS is induced in the lower Ni valence region by interaction with the ceramic O(2*p*)-band. The interface Zr ions are less perturbed by the presence of the interface; the valence band projections on Zr indicate they are coordinated to the interface oxygens. Metal-induced gap states (MIGS) are visible on both the surface O and Zr, but are barely present in the lower ceramic layers. The Fermi level aligns to the middle of the oxide gap.

In Table X we show charge and magnetic moment per ion, averaged over distinct layers. Table rows are ordered along the interface normal, so that the table provides a spatial profile. All data in this table are generated from the interface configuration with 3 layers ZrO_2 deposited onto a 3-layer Ni substrate, shown in Fig. 3(c). The four rightmost columns of Table X display induced charges and magnetic moment. ''Induced'' means that we have subtracted the charge or magnetic moment of the corresponding layers in either the isolated 3-layer ZrO_2 or Ni films (or in the bulk) from the charge or magnetic moment of the interface structure. These two distinct comparisons gives an idea of the impact the interface formation has on both surface and bulk electronic properties.

Compared to isolated films, the most noticeable change is that interface ions regain charge on interface formation, which previously spilled out into the vacuum. It appears some bonding charge in the interface region is drawn from upper part of the first ceramic layer (both O and Zr) and the first Ni layer and placed at the interface oxygen layer (which regains its bulk charge completely). The induced charges do not add up to zero, due to the vacuum region, neglect of the interstitial region, and sphere overlap, as pointed out above. The interface formation results in an even further depletion of the magnetic moment on the Ni-surface (which already has less magnetic moment than the Ni bulk). On the other hand, a small aligned magnetic moment is induced in the interface oxygen layer. Interestingly, an antialigned magnetic moment is also induced in the cations in the first ceramic layer, showing that they participate covalently in the interface bonding as well. Apart from this, Table X shows the interface formation has a minute effect on substrate/ceramic layers further from the interface, supporting the point that the overall interface chemistry is local.

In Table XI, we have resolved the DOS layer averages for the metallic/ceramic interface layers into particular ions. We use same convention for calculating induced charge (film or bulk reference state) as explained for Table X. Again the rows are ordered according to ionic position along the interface normal. The charge on Ni ions drops the closer they are to the interface plane, supporting the point that Ni donates some charge to interface oxygens. Interestingly, the magnetic moment on Ni ions increases, the closer they are to the interface plane, in contrast to the decrease in magnetic moment approaching the free Ni surface. This seems to correlate with the induced magnetic moment on interface oxygen, however. The interlayer resolution of charges reveal that $Zr^2(1)$ and $Zr^1(1)$ donate a little to $Ni^{1a}(1)$ and $Ni^2(1)$ (see Table VI

TABLE XI. Valence charge (electrons/ion) and magnetic moment (μ_B/ion (using the GGA) resolved onto interface ions in the unit cell for the interface configuration with 3 layers $ZrO_2(111)$ deposited onto 3 layers Ni(111). Induced charge and magnetic moment have same meaning as in Table X (see text for further details). Row order is according to position along interface normal. Ion type classification superscripts follow Table VI; ion numbers in parentheses label the frequency of a given type in the interface region per supercell.

Ion type	Absolute		Induced (vs film)		Induced (vs bulk)	
	Charge	Moment	Charge	Moment	Charge	Moment
$Zr^1(1)$	2.85	−0.03	0.05	−0.03	−0.04	−0.03
$Zr^1(2)$	2.79	−0.03	−0.01	−0.03	−0.11	−0.03
$Zr^2(1)$	2.79	−0.06	−0.01	−0.06	−0.10	−0.06
$O^1(1)$	6.40	0.02	0.11	0.02	−0.02	0.02
$O^1(2)$	6.41	0.02	0.11	0.02	−0.02	0.02
$O^3(1)$	6.46	0.08	0.17	0.08	0.04	0.08
			Interface			
$Ni^{1b}(1)$	9.39	0.61	0.02	−0.07	−0.13	−0.11
$Ni^{1b}(2)$	9.43	0.56	0.07	−0.12	−0.09	−0.16
$Ni^{1b}(3)$	9.51	0.62	0.15	−0.06	−0.01	−0.10
$Ni^2(1)$	9.47	0.56	0.11	−0.12	−0.05	−0.16
$Ni^{1a}(1)$	9.49	0.54	0.13	−0.13	−0.03	−0.17
$Ni^2(2)$	9.54	0.53	0.17	−0.15	0.02	−0.18
$Ni^{1a}(2)$	9.54	0.49	0.18	−0.19	0.02	−0.23

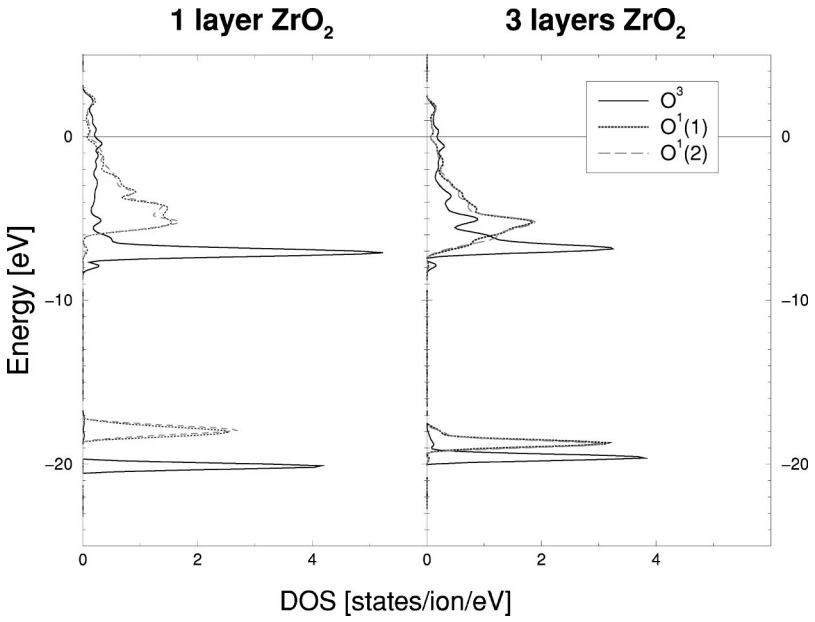

FIG. 5. Atom-projected DOS for interface anions, for 1 and 3 layers of ZrO_2 adsorbed, respectively (see Table VI for interface ion classification). The energy zero point is at the Fermi level for each interface structure.

for ion labeling) and that $Ni^{1b}(3)$ donates a little to $O^1(2)$; the hollow site oxygen $O^3(1)$ receives a slight amount of charge. So there is some internal charge redistribution in the vicinity of the interface, but no significant net transfer to or across the interface. This view is supported by the fact that the interslab dipole interaction energy is minute, as pointed out in Sec. III C. Calculations for other metal/ceramic systems has also suggested very little charge transfer across the interface.[69,73–75]

In Fig. 5 we show the atom-projected density of states for interface oxygen ions for the case of 1 and 3 layers of ZrO_2 adsorbed, respectively. The splitting of the O(2*s*) peaks between O^1 and O^3 type ions (see Table VI for interface ion classification) increases markedly for 1 layer vs 3 layers of ZrO_2: the O^3 ions for 1 layer of ZrO_2 are subjected to a deeper image potential from the Ni substrate; the O(2*s*) peaks track the electrostatic potential experienced by the anions, loosely speaking. The stronger electrostatic stabilization of O^3 ions causes the $O^3(2p)$ states to fall below the ceramic O(2*p*) valence band and localize (cf. the narrow peak). The interaction with the Ni substrate becomes more adsorbatelike. The O^1 ions still participate in the O(2*p*) valence band, as is visible from the strong weight the O(2*p*) valence band has on these ions. For 3 layers of ZrO_2, all interface anions are still ceramiclike, i.e., have dominant projections from the bulk O(2*p*) valence band. The weighted average one-electron potential for the interface oxygen layer is about the same for 1 and 3 layers of ZrO_2 adsorbed, respectively. For the ZrO_2 monolayer, the $O^1(2s)$ are higher than for 3 layers: this is associated with a charge redistribution in the interface oxygen layer. This is clearly revealed in Table XII, which shows that charge associated with O^3 is increased by ~0.11 electrons, whereas the charge associated O^1 ions is decreased with ~0.08 electrons.

TABLE XII. Comparison of charge (electrons/ion) on individual interface oxygen ions (for ion type classification superscripts, see Table VI) for 1 and 3 layers of ZrO_2(111) adsorbed, respectively. Also shown is the average charge of all interface Ni atoms.

Ion type	Interface oxygen charge (electrons/ion) 1 layer ZrO_2	3 layers ZrO_2
$O^1(1)$	6.32	6.40
$O^1(2)$	6.33	6.41
$O^3(1)$	6.57	6.46
Ni (layer average)	9.52	9.48

In Fig. 6 we compare the atom-projected density of states averaged over all interface Ni and oxygen ions for one and three layers of ZrO_2 adsorbed, respectively. The figure shows that the local Ni band width at the interface is increased for one layer, indicating increased covalency; it also shows a stronger $O^3(2p)$ peak for the ZrO_2 monolayer in the lower Ni valence band. All in all, this supports the view that for thick ceramic films the bonding is image-charge-driven, with interface anions being mostly ceramic like: the ceramic prefers internal bonding. For monolayer ZrO_2 films, some anions change character from ceramic to adsorbatelike and form localized bonds with the Ni substrate, causing an overall more covalent interface cohesion.

IV. CONCLUSIONS

We have used the ultrasoft pseudopotential DFT formalism to study the $Ni(111)\sqrt{7}\times\sqrt{7}\|c\text{-}ZrO_2(111)\sqrt{3}\times\sqrt{3}$ ideal interface in detail, as a model thermal barrier coating (TBC) system. The lattice constant mismatch is nominally 5%, but the tensile stress is released somewhat by an incomplete $c\rightarrow m\text{-}ZrO_2(111)$ phase transition in the ceramic layer. Our main finding is that $ZrO_2(111)$ adheres relatively strongly at the monolayer level, but thicker ceramic films interact weakly with the Ni-substrate. This reveals at least one reason why pure ZrO_2 is inadequate as a TBC, since the thick films needed as a thermal shield will be only weakly adhered, leading to easy spallation. A $ZrO_2(111)$ monolayer is predicted to have an ideal work of adhesion of 2000

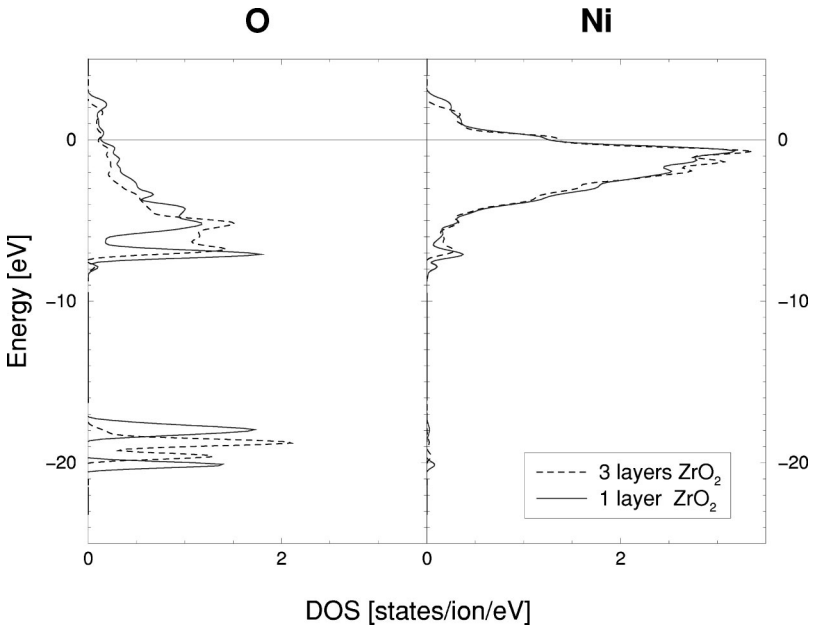

FIG. 6. Atom-projected DOS for interface Ni and O ions, averaged over their layers, for 1 and 3 layers of ZrO_2 adsorbed, respectively (see Table VI for interface ion classification). The energy zero point is at the Fermi level for each interface structure.

(2750) mJ/m^2 using the GGA (LSDA) for exchange-correlation effects. We extrapolate the ideal work of adhesion for an infinitely thick ZrO_2 layer to 750 mJ/m^2, with ceramic–ceramic bonds strengthened at the expense of the metal–ceramic bonds, when the ceramic layer grows.

This trend is opposite to what is expected from the simplest image charge interaction model,[67] which states that the major contribution to metal–ceramic bonding is the electrostatic attraction between the ceramic and its (oppositely-charged) image in the metal; a thicker ceramic layer would produce a larger (oppositely-charged) electrostatic image and thus bond stronger. This counterintuitive finding is due to the nature of interface bonding, which depends on the thickness of the ceramic film. For thick ceramic films, the bonding is image-charge-driven, with interface anions being mostly ceramiclike, whereas for monolayer ZrO_2 films, some anions change character from ceramic to adsorbatelike and form localized bonds with the Ni substrate, causing a more covalent interface cohesion. It will be quite a challenge in the future to construct a model potential metal–ceramic interaction reproducing this effect (for the right reason).

The $\mathrm{Ni}(111)\sqrt{7}\times\sqrt{7}\|c\text{-}\mathrm{ZrO_2}(111)\sqrt{3}\times\sqrt{3}$ interface unit cell has 9 bonds, 5 short Ni–O and 4 diffuse Ni–Zr bonds. The O contact sites on the Ni(111) substrate are threefold hollow and on-top, in the ratio 1:2. We attribute this to a geometric frustration, caused by the unequal point group symmetry and lattice constants of Ni(111) and $m\text{-}\mathrm{ZrO_2}(111)$. We find a significant rumpling of Ni substrate, caused by the adhesion of the ZrO_2 film. The ZrO_2 film attains a quasi monoclinic structure. The average bond energy is 0.52 (0.68) eV/bond for a single ceramic layer, using GGA (LSDA) decreasing to 0.2 eV/bond for an infinitely thick ceramic layer, using the GGA. We find no significant charge transfer across the interface, but some redistribution in the interface region. Also, our results show a depression of the magnetic moment at the interface Ni atoms, further below the magnetic moment depression at the Ni surface. A very slight magnetic moment is induced by Ni on the ZrO_2 interface ions, spin-parallel for anions and spin antiparallel for the cations. Our investigation has been limited to stoichiometric ZrO_2 deposited on Ni(111) for computational reasons. In the future it would be interesting to address off-stoichiometric effects at the Ni/ZrO_2 interface by first principles calculations.

We have demonstrated that a 3-layer Ni(111) slab is an adequate model for the infinite Ni(111) substrate, both from a structural and energetical point of view. The most severe limitation in our study is the imposition of periodic boundary conditions (PBC's). We have argued that the influence of PBC's tend to cancel out in energetic and structural *differences* induced by interface formation. Using a significantly larger interface unit cell to lessen the effects of PBC's is not feasible presently, using Kohn–Sham DFT methods. We find sensitivity on initial structure and translation of the deposited ZrO_2 film, so that several local minima exist on the interface potential energy surface. This complicates modeling of heterogeneous metal–ceramic interfaces.

To test the sensitivity of various approximations in DFT, we explored the bulk phases of Ni and ZrO_2. Concerning the exchange-correlation density functional parameterization (LSDA/GGA), the situation is somewhat unfortunate from a structural point of view: the LSDA predicts a perfect volume for ZrO_2, but underestimates the volume for Ni. On the other hand, the GGA overestimates the volume for ZrO_2, but yields a perfect volume for Ni. Relative structures and intracell features in the ZrO_2 polymorphs are better described using the GGA. Energetically, the LSDA underestimates structural energy differences between ZrO_2 polymorphs, whereas the GGA overestimates them.

Zr semicore states are necessary in some contexts to describe the chemistry of Zr appropriately. Although including Zr semicore states is formally less of an approximation, the importance of Zr semicore states for ZrO_2 is an open question. We find that the main effect of Zr semicore states is to

provide a uniform rescaling of volumes. Energetically, Zr semicore states have little effect, but provide minute improvements for LSDA. They correct perfectly the LSDA underestimation of volume by 1%. In conjunction with the GGA, they worsen the GGA tendency to overestimate volume and structural energy differences. We note that there is a fortuitous error cancellation in bond lengths between treating Zr semicore states within a frozen core approximation and the GGA for exchange-correlation effects. This error cancellation comes in handy in order to avoid artificial interface stress, due to the inadequateness of either parameterization (LSDA/GGA) of the exchange-correlation density functional.

ACKNOWLEDGMENTS

We are grateful to G. Kresse for helpful guidance with the VASP code. Further we wish to thank Niranjan Govind, Stuart C. Watson, Emily A. A. Jarvis, and M. A. van Hove for useful comments in the course of the work. We acknowledge also computing time granted on the parallel IBM SP2 platforms at the Maui High Performance Computing Center (MHPCC) and the Office of Academic Computing, UCLA. This work was supported by the Air Force Office of Scientific Research.

[1] A. Christensen, E. A. A. Jarvis, and E. A. Carter, in *Chemical Dynamics in Extreme Environments (Advanced Series in Physical Chemistry)*, edited by R. A. Dressler and C. Ng (World Scientific, Singapore, 2000).
[2] D. J. Wortman, B. A. Nagaraj, and E. C. Duderstadt, Mater. Sci. Eng., A **A120-1**, 433 (1989).
[3] S. M. Meier, D. K. Gupta, and K. D. Sheffler, J. Miner. Met. Mater. Soc. **43**, 50 (1991).
[4] E. Ryshkewitch and D. W. Richerson, *Oxide Ceramics* (Academic, Orlando, 1985).
[5] S. Musikant, *What Every Engineer Should Know About Ceramics* (Marcel Dekker, New York, 1991).
[6] F. Stott, D. de Wet, and R. Taylor, MRS Bull. **19**, 46 (1994).
[7] Y. Sohn, R. Biederman, and J. Sisson, J. Mater. Eng. Perform. **3**, 55 (1994).
[8] R. Taylor, J. Brandon, and P. Morrell, Surf. Coat. Technol. **50**, 141 (1992).
[9] A. E. Hughes, in *Science of Ceramic Interfaces II*, edited by J. Nowotny (Elsevier, Amsterdam, 1994).
[10] W. Lih, E. Chang, B. Wu, and C. Chao, Oxid. Met. **36**, 221 (1991).
[11] R. A. Miller, J. Am. Ceram. Soc. **67**, 517 (1984).
[12] S. Aruna, M. Muthurama, and K. Patil, Solid State Ionics **111**, 45 (1998).
[13] U. Flesch, J. Meusinger, A. Naoumidis, and D. Stover, Mater. Sci. Forum **308**, 788 (1999).
[14] C.-H. Lee, C.-H. Lee, H.-Y. Lee, and S. Oh, Solid State Ion. Diff. React. **98**, 39 (1997).
[15] M. Fukumoto *et al.*, J. Jpn. Inst. Met. **58**, 50 (1994).
[16] S. Primdahl and M. Mogensen, J. Appl. Electrochem. **30**, 247 (2000).
[17] D. Simwonis *et al.*, J. Mater. Process. Technol. **92**, 107 (1999).
[18] A. Christensen and E. A. Carter, Phys. Rev. B **62**, 16968 (2000).
[19] E. A. A. Jarvis, A. Christensen, and E. A. Carter, Surf. Sci. (submitted).
[20] A. Christensen and E. A. Carter, Phys. Rev. B **58**, 8050 (1998).
[21] D. Vanderbilt, Phys. Rev. B **41**, 7892 (1990).
[22] K. Laasonen, R. Car, C. Lee, and D. Vanderbilt, Phys. Rev. B **43**, 6796 (1991).
[23] K. Laasonen *et al.*, Phys. Rev. B **47**, 10142 (1993).
[24] P. Hohenberg and W. Kohn, Phys. Rev. B **136**, 864 (1964).
[25] W. Kohn and L. J. Sham, Phys. Rev. A **140**, 1133 (1965).
[26] U. von Barth and L. Hedin, J. Phys. C **5**, 1629 (1972).
[27] G. Parr and W. Yang, *Density-Functional Theory of Atoms and Molecules* (Oxford University Press, New York, 1989).
[28] G. Kresse and J. Hafner, Phys. Rev. B **47**, 558 (1993).
[29] G. Kresse and J. Hafner, Phys. Rev. B **49**, 14251 (1994).
[30] G. Kresse and J. Furthmüller, Comput. Mater. Sci. **6**, 15 (1996).
[31] G. Kresse and J. Furthmüller, Phys. Rev. B **54**, 11169 (1996).
[32] L. Kleinman and D. M. Bylander, Phys. Rev. Lett. **48**, 1425 (1982).
[33] A. M. Rappe, K. M. Rabe, E. Kaxiras, and J. D. Joannopoulos, Phys. Rev. B **41**, 1227 (1990).
[34] G. Kresse and J. Hafner, J. Phys.: Condens. Matter **6**, 8245 (1994).
[35] J. P. Perdew and A. Zunger, Phys. Rev. B **23**, 5048 (1981).
[36] D. M. Ceperley and B. J. Alder, Phys. Rev. Lett. **45**, 566 (1980).
[37] J. P. Perdew, in *Electronic Structure of Solids*, edited by P. Ziesche and H. Eschrig (Akademie Verlag, Berlin, 1991), p. 11.
[38] J. P. Perdew *et al.*, Phys. Rev. B **46**, 6671 (1992).
[39] H. J. Monkhorst and J. D. Pack, Phys. Rev. B **13**, 5188 (1976).
[40] M. Methfessel and A. T. Paxton, Phys. Rev. B **40**, 3616 (1989).
[41] P. Pulay, Chem. Phys. Lett. **73**, 393 (1980).
[42] M. Fuchs, M. Bockstedte, E. Pehlke, and M. Scheffler, Phys. Rev. B **57**, 2134 (1998).
[43] R. King-Smith, M. Payne, and J. Liu, Phys. Rev. B **44**, 13063 (1991).
[44] G. Makov and M. C. Payne, Phys. Rev. B **51**, 4014 (1995).
[45] J. Neugebauer and M. Scheffler, Phys. Rev. B **46**, 16067 (1992).
[46] A. Bogicevic and D. R. Jennison, Phys. Rev. Lett. **82**, 4050 (1999).
[47] E. G. Moroni, G. Kresse, J. Hafner, and J. Furthmüller, Phys. Rev. B **56**, 15629 (1997).
[48] H. Herper, E. Hoffmann, and P. Entel, J. Phys. IV **7**, 71 (1997).
[49] B. Barbiellini, E. Moroni, and T. Jarlborg, J. Phys.: Condens. Matter **2**, 7597 (1990).
[50] V. Moruzzi, A. Williams, and J. Janak, Phys. Rev. B **15**, 2854 (1977).
[51] P. Bagno, O. Jepsen, and O. Gunnarsson, Phys. Rev. B **40**, 1997 (1989).
[52] V. Ozolins and M. Körling, Phys. Rev. B **48**, 18304 (1993).
[53] G. Jomard *et al.*, Phys. Rev. B **59**, 4044 (1999).
[54] N. Troullier and J. L. Martins, Phys. Rev. B **43**, 1993 (1991).
[55] J. P. Perdew, Phys. Rev. B **33**, 8822 (1986).
[56] A. D. Becke, J. Chem. Phys. **96**, 2155 (1992).
[57] G. Stapper, M. Bernasconi, N. Nicoloso, and M. Parrinello, Phys. Rev. B **59**, 797 (1999).
[58] B. Hammer, L. Hansen, and J. Norskov, Phys. Rev. B **59**, 7413 (1999).
[59] C. T. Campbell, Surf. Sci. Rep. **27**, 1 (1997).
[60] B. C. Bolding and E. A. Carter, Mol. Simul. **9**, 269 (1992).
[61] U. Schonberger, O. K. Andersen, and M. Methfessel, Acta Metall. Mater. S **40**, 1 (1992).
[62] A. Christensen and E. A. Carter (unpublished).
[63] D. Vu, K. Michell, O. Warren, and P. Thiel, Surf. Sci. **318**, 129 (1994).
[64] H. Zeng and K. Mitchell, Surf. Sci. **239**, L571 (1990).
[65] R. Headrick, P. Konarski, S. Yalisove, and W. Graham, Phys. Rev. B **39**, 5713 (1989).
[66] N. Ting, Y. Qingliang, and Y. Yiying, Surf. Sci. **206**, L857 (1988).
[67] M. W. Finnis, J. Phys.: Condens. Matter **8**, 5811 (1996).
[68] V. Musolino, A. Selloni, and R. Car, Surf. Sci. **402-404**, 413 (1998).
[69] G. Pacchioni and N. Rosch, J. Chem. Phys. **104**, 7329 (1996).
[70] J. G. Duh and W. S. Chien, J. Mater. Sci. **25**, 1529 (1990).
[71] W. Wang *et al.*, J. Mater. Sci. **35**, 1495 (2000).
[72] A. Tsoga, A. Naoumidis, and P. Nikolopoulos, Acta Mater. **44**, 3679 (1996).
[73] I. Yudanov, G. Pacchioni, K. Neyman, and N. Rosch, J. Phys. Chem. B **101**, 2786 (1997).
[74] A. Matveev, K. Neyman, G. Pacchioni, and N. Rosch, Chem. Phys. Lett. **299**, 603 (1999).
[75] I. Yudanov *et al.*, Chem. Phys. Lett. **275**, 245 (1997).
[76] C. Kittel, *Introduction to Solid State Physics* (Wiley, New York, 1996).
[77] H. G. Scott, J. Mater. Sci. **10**, 1527 (1975).
[78] P. Aldebert and J.-P. Traverse, J. Am. Ceram. Soc. **68**, 34 (1985).
[79] C. J. Howard, R. J. Hill, and B. E. Reichert, Acta Crystallogr., Sect. B: Struct. Sci. **44**, 116 (1988).
[80] R. Stevens, Technical Report, Magnesium Electron Ltd. (unpublished).
[81] R. J. Ackermann, E. G. Rauh, and C. A. Alexander, High. Temp. Sci. **7**, 304 (1975).
[82] R. Orlando, C. Pisani, C. Roetti, and E. Stefanovich, Phys. Rev. B **45**, 592 (1992).